

A Simple Approach for Specifying Velocity Inflow Boundary Conditions in Simulations of Turbulent Opposed-Jet Flows

Ranjith R. Tirunagari · Michael W. A. Pettit ·
Andreas M. Kempf · Stephen B. Pope

Received: date / Accepted: date

Abstract A new methodology is developed to specify inflow boundary conditions for the velocity field at the nozzle exit planes in turbulent counterflow simulations. The turbulent counterflow configuration consists of two coaxial opposed nozzles which emit highly-turbulent streams of varying species compositions depending on the mode considered. The specification of velocity inflow boundary conditions at the nozzle exits in the counterflow configuration is non-trivial because of the unique turbulence field generated by the turbulence generating plates (TGPs) upstream of the nozzle exits. In the method presented here, a single high-fidelity large-eddy simulation (LES) is performed in a large domain that spans the region between the TGPs of the nozzles, and the time series of the velocity fields at the nozzle exit planes are recorded. To provide inflow boundary conditions at the nozzle exit planes for simulations under other conditions (e.g., different stream compositions, bulk velocity, TGP location), transformations are performed on the recorded time series: the mean and r.m.s. (root-mean-square) quantities of velocity, as well as the longitudinal integral length scale on the centerline, at the nozzle exits in simulations are matched to those observed in experiments, thereby matching the turbulent Reynolds number Re_t . The method is assessed by implementing it in coupled large-eddy simulation/probability density function (LES/PDF) simulations on a small cylindrical domain between the nozzle exit planes for three different modes of the counterflow configuration: N_2 vs. N_2 ; N_2 vs. hot combustion products; and CH_4/N_2 vs. O_2 . The inflow method is found to be successful as the first and second moments of velocity from the LES/PDF simulations agree well with the experimental data on the centerline for all three modes. This simple yet robust inflow strategy can be applied to eliminate the computational cost required to simulate the flow field upstream of the nozzle exits. It is also emphasized that, in addition to the predicted time series data, the availability of experimental data close to the nozzle exit planes plays a key role in the success of this method.

Keywords Turbulent counterflow simulations · Velocity inflow boundary conditions · LES/PDF · Auto-correlation function · Velocity statistics

R.R. Tirunagari[†] · S.B. Pope
Sibley School of Mechanical and Aerospace Engineering, Cornell University,
Ithaca, NY 14853, USA
[†]E-mail: rrt38@cornell.edu

M.W.A. Pettit
Department of Mechanical Engineering, Imperial College London,
South Kensington Campus, Exhibition Road, London SW7 2AZ, United Kingdom

A.M. Kempf
Institute for Combustion and Gas Dynamics (IVG) and Center for Computational Sciences and Simulation,
Universität Duisburg-Essen, Duisburg 47048, Germany

1 Introduction

Turbulent counterflow flames (TCFs) were experimentally studied in the early 1990s in terms of their flame structure, fundamental combustion processes and extinction limits in non-premixed and premixed modes, to evaluate the potential of this configuration for combustion research and to establish a foundation for computational investigations [1–3]. More recently, TCFs have been considered as an alternative to the well-known jet flames as a configuration in which to study fundamental processes in turbulent combustion. It is well demonstrated and documented in [4–8] that the TCF configuration offers several advantages for the study of turbulence-chemistry interactions in a laboratory arrangement. Some of the key advantages are: (i) the achievement of high Reynolds numbers without pilot flames; (ii) the range of combustion regimes that can be realized, from stable flames to local extinction/re-ignition conditions; (iii) the compactness of the domain compared to jet flames; (iv) the ability to explore a variety of fuels, including bio-fuels and fuel blends; and (v) the relevance to practical combustion devices in terms of operating conditions.

The main motivation of the collaborative TCF studies has been to test the computational models of mixing [9, 10], turbulence [11] and combustion [4] by performing detailed comparisons to experimental data for flow and scalar fields. The computational work described in this paper is part of a collaborative project which aims at studying TCFs using both experimental and computational techniques. A series of experiments on TCFs, operating in non-reactive, non-premixed and premixed modes, were performed at Yale University and at Sandia National Laboratories [12, 13]; and the same flames are being studied computationally using the large-eddy simulation/probability density function (LES/PDF) methodology [14–16].

1.1 The turbulent counterflow flame (TCF) configuration

The counterflow configuration shown in Fig. 1 consists of two coaxial opposed nozzles of diameter $d_{jet} = 12.7$ mm placed at a variable distance d apart. The nozzles are surrounded by an annular co-flow of N_2 with an outer diameter of 29.5 mm. This configuration can be operated in different modes and we considered three modes in this paper as follows:

- *Inert/Inert (I/I) mode*: both nozzles emit highly-turbulent streams of N_2 gas at temperature $T_u = 294$ K and pressure 1 atm., leading to a non-reactive flow with inert mixing.
- *Inert/Burnt (I/B) mode*: the top nozzle emits a highly-turbulent stream of N_2 at $T_u = 294$ K and 1 atm., while the bottom nozzle emits burnt stoichiometric combustion products at $T_b = 1850$ K and 1 atm., leading to an essentially non-reactive flow with mixing between the inert gas and hot combustion products.
- *Fuel/Oxidant (F/O) mode*: the top nozzle emits a highly-turbulent stream of oxidant in the form of pure O_2 at $T_u = 294$ K and 1 atm. and the bottom nozzle emits a highly-turbulent stream of diluted fuel in the form of CH_4/N_2 at a molar ratio of 35:65 at $T_u = 294$ K and 1 atm., leading to a non-premixed flame sandwiched between the two nozzles.

The experimental configuration for the I/I and F/O modes is shown in Fig. 1(a) and for the I/B mode in Fig. 1(b). The configuration for the I/B mode is different in that the bottom nozzle hosts a pre-burner which burns a stoichiometric fuel-air mixture ($CH_4/O_2/N_2$ with a molar ratio of 26:74 for O_2/N_2) to completion to generate the stream of hot combustion products. It is important to note that all the streams operated in the above modes are highly-turbulent except for the combustion product stream in the I/B mode. The hot stream of combustion products has high viscosity and therefore the turbulence generating plate (TGP) is removed from the corresponding nozzle. More experimental details of these modes can be found in [12, 13].

As highlighted in Fig. 1(b), each nozzle (except the bottom nozzle in the I/B mode) houses a high-blockage TGP [17] which generates a high-intensity turbulence field at the nozzle exit. The stream forms a high-speed jet as it passes through the TGP, which breaks up into a complex, highly-turbulent flow with strong re-circulation effects in the contraction zone prior to exiting the nozzle. The turbulence that is observed in the region between the two nozzles

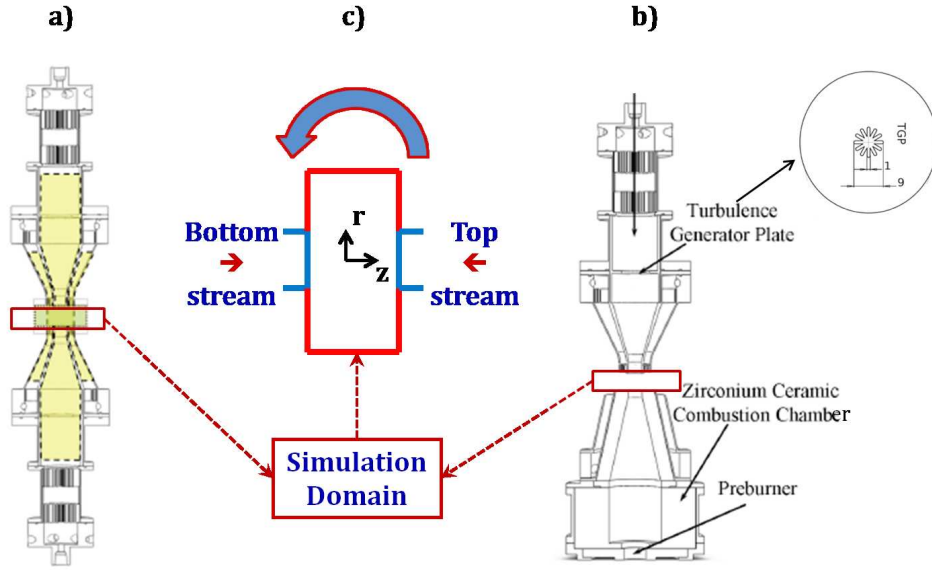


Fig. 1: The experimental configuration for (a) the I/I and F/O modes, (b) the I/B mode, and (c) the computational domain used in the LES/PDF simulations. The domain in (c) is shown such that the bottom stream is on the LHS and the top stream is on the RHS. The computational domain aligns with the experimental configurations when it is rotated by 90° in the anti-clockwise direction as indicated by the arrow. The computational domain used in the single large-domain LES is marked in green color in (a), whereas the computational domain used in the small-domain LES/PDF simulations is highlighted by red box in (a) and (b).

is largely determined by the turbulence generating mechanism of the TGP in the contraction zone.

1.2 Choice of LES solution domain

There have been many collaborations in the past involving experimental and numerical studies of the TCF configuration (e.g., [4, 12, 18]). One of the underlying aspects in these studies is the choice of the computational domain. The two computational domains that have been used are, broadly: (i) a large domain that *includes* the upstream region of the nozzle exits *as well as* the region between them, as shown in green color in Fig. 1(a); and, (ii) a small cylindrical domain that includes *only* the region between the two nozzle exits, and therefore *excludes* the upstream region involving the TGP, as depicted in red color in Fig. 1(a) and shown in Fig. 1(c).

In many previous studies involving high-fidelity LES of the counterflow configuration (e.g., [4, 12]), a large computational domain is chosen, which includes the region upstream of the nozzle exits. The main advantage of choosing such a computational domain is that it facilitates the prediction of the development of the flow and turbulence field downstream of the TGP. Hence, such simulations are predictive. Additionally, the boundary conditions for the velocity field at the inflow boundaries of the large domain are simpler, i.e., non-turbulent, and we suppose that the conditions at the nozzle exits are insensitive to the details of these specified boundary conditions. However, the large computational domain and the complex geometry make the LES calculations difficult and expensive. Although the prediction of the velocity field downstream of the TGP is important, the main focus of the counterflow studies has been

to understand turbulence-chemistry interactions in the region between the two nozzle exit planes, where a turbulent non-premixed/premixed flame is established near the mid-plane. It is therefore logical to consider the second choice – a smaller cylindrical computational domain between the two nozzle exits. Due to its simple geometry and smaller size, this solution domain enables simpler and less expensive high-fidelity LES. On the other hand, one major limitation of choosing such a compact domain is the need to specify inflow boundary conditions on the (turbulent) velocity field at the nozzle exit planes. It was concluded early on in previous counterflow studies that predicting the turbulent velocity field in the downstream region of the TGP is essential to choosing the correct boundary conditions at the nozzle exit planes [19].

1.3 Objectives and challenges

In this work, we present results from the LES/PDF simulations of the three operating modes described in Sec. 1.1 on a small cylindrical domain that encompasses the volume between the two nozzle exit planes as shown in Fig. 1(c). The solution domain has two inflows in the axial direction for the two opposed streams and an outflow in the radial direction. The coupled LES/PDF simulations are computationally expensive primarily due to the Monte-Carlo particle based PDF code, and more importantly the prime focus is to study the turbulence-chemistry interactions in the turbulent flames which are established near the stagnation plane. Therefore, it is decided to consider the small solution domain excluding the nozzles to make the high-fidelity LES/PDF simulations simpler and less expensive.

It then becomes imperative to specify realistic velocity inflow boundary conditions at the exit planes that mimic the conditions observed in the experiments. For example, the velocity field data generated by simulating the turbulent flow in a simple pipe is not adequate to represent the complex perturbations imposed by the TGP on the turbulence field at the nozzle exit. In particular, the turbulence intensity generated from a pipe flow is much lower than that obtained at the nozzle exit when using the TGP inside the nozzle.

The main objective of this work is to address the issue of providing velocity boundary conditions at the inflow boundaries (i.e., nozzle exit planes) of this small computational domain to facilitate LES/PDF simulations of turbulent flows/flames in TCFs.

The remainder of the paper is organized as follows. In Sec. 2, we describe the methodology for specifying the velocity inflow boundary conditions. In Sec. 3, the inflow method is applied in the LES/PDF simulations involving the non-reactive and non-premixed modes described in Sec. 1.1: we describe the computational methodology and the key simulation parameters, followed by a discussion on the comparisons of velocity statistics on the centerline and across the nozzle exits with the experimental data for all the modes. Finally, conclusions from this study are summarized in Sec. 4.

2 Inflow boundary conditions methodology

We present a methodology to address the issue of specifying velocity inflow boundary conditions at the nozzle exit planes for the small cylindrical domain used in the LES/PDF simulations. The three key components of this methodology are:

- A single high-fidelity LES on the large domain, which includes the TGP, as shown in green color in Fig. 1(a), to obtain and record the time series of the velocity components at the nozzle exit planes.
- The existing experimental data [12, 13] on the mean and r.m.s. (root-mean-square) axial and radial velocity components, and the longitudinal integral length scale on the centerline near the nozzle exit planes.
- A transformation procedure that is used on the recorded exit-plane data to form velocity inflow boundary conditions for use in the LES/PDF simulations on the small domain, shown in Fig. 1(c). The transformations are performed so that key statistics of the inflowing velocity fields match those measured in the experiments.

In the following sub-sections, we describe these three components of the methodology in more detail.

2.1 Single large-domain LES

The non-reactive case of the I/I mode is simulated in the large computational domain (shown in Fig. 1(a)) in order to collect the time series of the velocity field at the nozzle exit planes. The burner geometry is described using immersed boundary conditions and the computational domain spans the entire region between the two TGP of the nozzles. As a result, the evolution of the turbulent jet downstream of each TGP nozzle is calculated. The conditions used in the simulations are listed under the Inert/Inert mode in Table 1. The large-domain LES is performed in Cartesian coordinates using the ‘PsiPhi’ LES/DNS code; more details about the implementation of the code and the results can be found in [12]. The uniform grid resolution used in the simulation is $h = 0.5$ mm, corresponding to a total number of 3.7M grid cells (where $1\text{M} = 10^6$). It is found that the simulation (from specified initial conditions) reaches a statistically-stationary state after 100 ms. The time series of the three components of velocity on both nozzle exit planes are then recorded for 500 ms. Specifically, the velocities are recorded for the two 26×26 sub-meshes that cover the exits of the 12.7 mm diameter nozzles.

2.2 Experiments

The experiments were performed on this counterflow configuration in the three modes at Yale University and at Sandia National Laboratories [12, 13]. The radial profiles of the mean and r.m.s. of axial and radial components of velocity, and longitudinal integral length scale on the centerline, are measured at a distance of 0.5 mm downstream of the nozzle exits. Additionally, experimental data are also available for velocity statistics (for all operating modes), and for OH mass fraction in the F/O mode, on the centerline connecting the two nozzles.

2.3 Transformation procedure

The time series of the velocity fields collected at the nozzle exit planes from the large-domain LES described in Sec. 2.1 are suitably transformed and used as boundary conditions at the inflow boundaries of the small cylindrical domain. In the following, we describe the treatment at the bottom nozzle exit plane. The treatment at the bottom nozzle exit plane is exactly the same in the I/I and F/O modes, whereas the treatment at the bottom nozzle exit plane in the I/B mode is described in Sec. 2.5. The procedure involves the following four transformations:

1. The velocities from the large-domain LES are transformed to the polar cylindrical coordinates used in the LES/PDF simulations. Thus $U_i^\ell(r, \theta, t)$ denotes the time series of the i^{th} component of the instantaneous velocity in the cylindrical coordinates at the nozzle exit plane obtained from the large-domain LES after this transformation. The axial, radial and azimuthal velocities are denoted by $i = 1, 2$ and 3 , respectively.
2. The axial and radial velocities are subjected to an r -dependent shift to match the measured mean velocity profiles.
3. The fluctuating components of velocity are subjected to an r -dependent scaling to match the measured r.m.s. velocities.
4. Time is stretched or compressed to match the longitudinal integral length scale on the centerline.

With $U_i^s(r, \theta, t)$ denoting the specified inflow velocities at the nozzle exit planes, the transformation procedure is as follows:

$$U_i^s(r, \theta, t) = \langle U_i(r) \rangle_m + \alpha_i(r) \left[U_i^\ell(r, \theta, \beta t) - \langle U_i^\ell(r) \rangle \right]. \quad (1)$$

With the above transformation procedure, the statistics of the modified time series $U_i^s(r, \theta, t)$ are closely matched to the corresponding statistics measured at a distance of 0.5 mm downstream of the nozzle exit plane in the experiments. The statistics that are matched are:

- The mean of the modified time series, $\langle U_i^s(r) \rangle$, is equal to the measured mean in the experiments, $\langle U_i(r) \rangle_m$.
- The parameter $\alpha_i(r)$ scales the fluctuations so as to closely match the r.m.s. axial and radial velocities of the modified time series to those measured in the experiments. Due to the lack of experimental data on the r.m.s. velocity in the azimuthal direction, $\alpha_3(r)$ is taken to be equal to $\alpha_2(r)$.
- The parameter β stretches time so as to closely match the longitudinal integral length scale on the centerline at the nozzle exit plane of the modified time series to that measured on the centerline at a distance of 0.5 mm downstream of the exit plane in the experiments. Note that the time series of all the velocity components are stretched with the same scaling factor.

Thus $U_i^s(r, \theta, t)$ is the modified time series of velocity at the nozzle exit plane, in cylindrical coordinates, whose mean and r.m.s. axial and radial velocity profiles, and longitudinal integral length scale on the centerline, closely match the corresponding quantities measured at 0.5 mm downstream of the exit plane in the experiments.

In the subsequent exposition, we show how Eq. 1 is applied to the time series data of the velocity fields at the bottom nozzle exit plane from the large-domain LES, in order to obtain the modified velocity time series data that can be used in the LES/PDF simulation of the I/I mode. It should be noted that although the large-domain LES is performed for the I/I mode, the predicted r.m.s. quantities at the nozzle exit planes do not exactly match the measured values in the experiments. Hence, under the same conditions, we apply the transformation procedure to the collected time series data even for this case.

Figure 2 shows the radial profiles of the mean and r.m.s. axial and radial velocity components of the modified velocity time series data at the nozzle exit plane. It is clear from this figure that the mean quantities match very well with the experimental data for all values of r/R as we directly impose the mean profiles from the experiments. The scaling parameters, $\alpha_1(r)$ and $\alpha_2(r)$ (with $\alpha_3(r) = \alpha_2(r)$), are taken as quadratic and cubic polynomials, respectively. These low-order polynomials are chosen as they provide smooth specifications of $\alpha_i(r)$, which can simply be obtained by solving a linear system of equations. With the scaling parameters $\alpha_i(r)$, we are able to match the r.m.s. quantities well with the experimental data for values of r/R up to 0.8 for the axial r.m.s. velocity and up to 0.6 for the radial r.m.s. velocity. It is important to match the r.m.s. quantities at the centerline ($r/R = 0$) and the mismatch away from the centerline has little effect on the centerline results from the LES/PDF simulations. It is worth noting the significant turbulence intensities on the centerline of 40% (axial) and 28% (radial) that are characteristic of the present TCF configuration.

2.4 Matching the longitudinal integral length scale of turbulence

In the experiments, the longitudinal integral length scale is measured on the centerline at a distance of 0.5 mm from the nozzle exit plane. The time series of the velocity at the nozzle exit plane from the large-domain LES (i.e., $U_i^\ell(r, \theta, t)$) are stretched (or compressed) in order to match the longitudinal integral length scale (on the centerline at the nozzle exit plane) of the modified time series to that measured in the experiments. We now describe the stretching method.

Consider the axial component of the centerline velocity at the nozzle exit plane from the large-domain LES, $U_1^\ell(0, \theta, t)$. It is noted that this quantity is independent of θ . We then define $u(t)$, the velocity fluctuation at this location, by:

$$u(t) = U_1^\ell(0, \theta, t) - \langle U_1^\ell(0, \theta, t) \rangle. \quad (2)$$

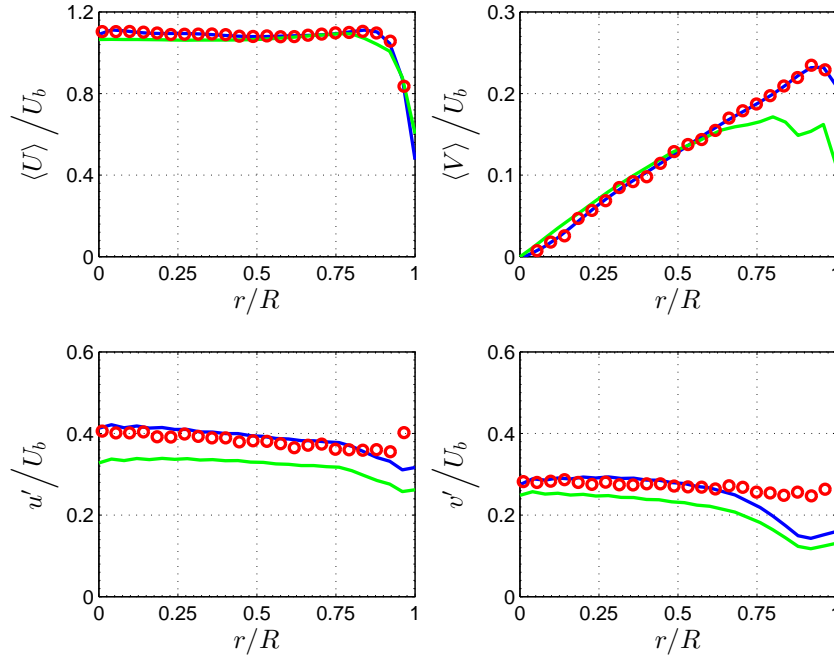


Fig. 2: The radial profiles of the mean (top row) and r.m.s. (bottom row) axial and radial velocities across the nozzle exit plane for the I/I mode; blue line: modified time series data as derived in Sec. 2.3, green line: large-domain LES (Sec. 2.1), red symbols: experimental data at 0.5 mm downstream of the nozzle exit plane [12].

The longitudinal auto-correlation function (LACF) $\rho_L(s)$ is defined based on $u(t)$ as follows:

$$\rho_L(s) = \frac{\langle u(t)u(t+s) \rangle}{\langle u(t)^2 \rangle}. \quad (3)$$

The entire 500 ms of data from the large-domain time series are used to calculate the LACF, which is shown in Fig. 3(a) for time increments up to 20 ms. From the LACF, the corresponding time scale $\tau(t)$ can be calculated as a function of time as:

$$\tau(t) = \int_0^t \rho_L(s) ds. \quad (4)$$

Figure 3(b) shows $\tau(t)$ for time increments up to 20 ms. The time scale $\tau(t)$ is subject to statistical sampling errors which increase with t , as may be evident from Fig. 3(a). While the definition of the longitudinal integral time scale is $\tau_L = \tau(\infty)$, a practical means of estimating τ_L from a finite time series is needed. Accordingly we estimate τ_L as the value of the integral in Eq. 4 at 20 ms, i.e., $\tau_L \approx \tau(0.02)$. Therefore, from Fig. 3(b), the value of τ_L for the large-domain LES velocity data is taken as 0.75 ms.

For the small-domain LES, the fluctuating component of the centerline axial velocity at the nozzle exit plane is specified (from Eq. 1) as:

$$u^s(t) = \alpha_1(0) u(\beta t). \quad (5)$$

It follows that the longitudinal integral time scale of $u^s(t)$, τ_L^s , is related to that of $u(t)$ by $\tau_L^s = \tau_L/\beta$. Thus, in order to match the measured longitudinal integral time scale, τ_L^m , the stretching factor β is specified as:

$$\beta = \frac{\tau_L}{\tau_L^m}. \quad (6)$$

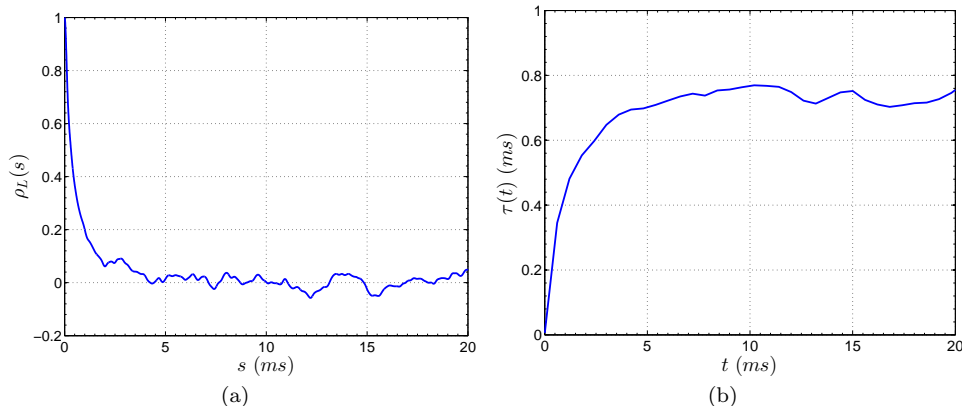


Fig. 3: (a) The longitudinal auto-correlation function (LACF) $\rho_L(s)$ based on the centerline axial velocity at the nozzle exit plane and (b) the corresponding integral time scale $\tau(t)$ as a function of time. The time series from the large-domain LES (Sec. 2.1) are used.

The longitudinal integral length scale ℓ_L^m observed in the experiments for the I/I mode is 3.6 mm, which corresponds to a longitudinal integral time scale τ_L^m of 0.55 ms from the relation:

$$\ell_L^m = \langle U_1(0) \rangle_m \tau_L^m. \quad (7)$$

Using the values of τ_L , τ_L^m and Eq. 6, a value of approximately 1.36 is obtained for β . (This is verified by stretching the large-domain LES time series velocity data by this factor β and recalculating the longitudinal integral time scale on the centerline at the nozzle exit plane for the modified time series data.)

It is noted that the Eulerian time scales of all velocity components are scaled by β^{-1} ; however only the axial length scales are affected and the two point correlations in the nozzle exit plane are unaltered.

The two key quantities that we match through the (fluctuation) scaling and (time) stretching methods are the axial r.m.s. velocity and the longitudinal integral length scale on the centerline at the nozzle exit plane to those measured at 0.5 mm downstream of the nozzle exit in the experiments. Therefore, we are able to match the turbulent Reynolds number Re_t in the simulations to that of the experiments for the I/I mode (see Eq. 12, Sec. 3.2).

Note that the above procedure is applied to the time series data from the large-domain LES at the bottom nozzle exit plane; a similar procedure can be followed to obtain the modified time series data at the top nozzle exit plane.

It is evident that the time series of the velocity field and the experimental data at (or close to) the nozzle exit planes play key roles in the success of this method. It is also important to note that the transformations are performed on the recorded data at the exit planes from the large-domain LES to obtain the velocity inflow boundary conditions for the LES/PDF simulations of all the three modes. Therefore, only a single large-domain LES is required for this method to be applied. Finally we conclude this section by acknowledging that as far as the velocity and turbulence fields at the inflow boundaries are concerned, the method is not predictive; however, it enables realistic simulations of these fields so that the combustion between the two nozzle exit planes can be studied.

2.5 Inflow boundary conditions for the burnt stream of the Inert/Burnt (I/B) mode

With the exception of the bottom nozzle in the I/B mode, the velocity inflow boundary conditions for all the turbulent streams of the three operating modes are generated using the

methodology described in Sec. 2.3 (Eq. 1). The bottom nozzle in the I/B mode is unique in that it does not emit a turbulent stream due to the absence of a TGP; additionally, there are no experimental data available close to the exit plane. Therefore, we considered two Cases (I and II) to impose the velocity inflow boundary conditions for the burnt stream emanating from the bottom nozzle exit in the I/B mode. Henceforth, we denote the bottom nozzle exit plane as $z = -z_e$ and the top nozzle exit plane as $z = z_e$ to differentiate between the two nozzles.

In Case I, the burnt stream is represented as a steady flow (velocity fluctuations are zero in all directions). This assumption is motivated by the absence of the TGP inside the bottom nozzle and the large viscosity of the hot products. The closest data points recorded in the experiments are at a distance of 3 mm above the bottom nozzle exit plane (i.e., $z = -z_e + 3$ mm), as accurate measurements could not be made at the hot combustion products stream nozzle exit (i.e., $z = -z_e$). The measured radial profiles of the mean axial and radial velocities are scaled to obtain the specified velocity profiles for the burnt stream at $z = -z_e$ for Case I. This is achieved as follows:

$$U_1^s(r, \theta, t) = \gamma_1 \langle U_1(r) \rangle_m, \quad (8a)$$

$$U_2^s(r, \theta, t) = \gamma_2 \langle U_2(r) \rangle_m, \quad (8b)$$

$$U_3^s(r, \theta, t) = 0. \quad (8c)$$

where $\langle U_1(r) \rangle_m$ and $\langle U_2(r) \rangle_m$ are the measured radial profiles of the mean axial and radial velocities, respectively, at $z = -z_e + 3$ mm in the experiments for the I/B mode. The scaling factor γ_1 for the mean axial velocity is chosen so that the volume flow rate is matched to that of the experiments, and the scaling factor γ_2 for the mean radial velocity is chosen so that the mean stagnation plane is at the mid-plane (as it is in the experiments).

In Case II, in addition to the mean profiles, “artificial” turbulence is imposed in all three directions by using Eq. 1. In experiments, it is observed that the burnt stream has large-scale, irrotational fluctuations, caused by the fluctuating pressure field generated by the turbulent flow from the top nozzle. Therefore, Case II is motivated by the presence of non-zero values of the turbulence intensities in the axial and radial directions in the experimental data at $z = -z_e + 3$ mm. The last two data points of the measured intensities (axial and radial) on the centerline near $z = -z_e + 3$ mm are used in a linear extrapolation to obtain the intensities on the centerline at $z = -z_e$. The ratio between the extrapolated centerline axial r.m.s. velocity at $z = -z_e$ and the measured centerline axial r.m.s. velocity at $z = -z_e + 3$ mm is used to scale the radial profile of the axial fluctuating velocity at $z = -z_e + 3$ mm to obtain the corresponding radial profile at $z = -z_e$. (The same procedure is followed for the radial fluctuating velocity.)

The specified velocity profiles for the burnt stream at $z = -z_e$ for Case II are as follows:

$$U_i^s(r, \theta, t) = \gamma_i \langle U_i(r) \rangle_m + \alpha_i(r) \left[U_i^\ell(r, \theta, t) - \langle U_i^\ell(r) \rangle \right]. \quad (9)$$

In Eq. 9:

- The axial, radial and azimuthal components of the velocity field are denoted by $i = 1, 2$ and 3, respectively.
- The scaling parameters for the mean axial and radial velocities, γ_1 and γ_2 , are obtained as described for Case I.
- The scaling parameter for the mean velocity in the azimuthal direction γ_3 is equal to 0.
- The scaling parameters α_1 and α_2 match the axial and radial r.m.s. velocities at $z = -z_e$ to the corresponding approximate experimental quantities, which are extrapolated from the measurements taken at $z = -z_e + 3$ mm.
- The scaling parameter α_3 is taken to be equal to α_2 due to the lack of experimental data for the r.m.s. velocity in the azimuthal direction.
- The stretching factor β is not applied due to the lack of experimental data for the longitudinal integral length scale, either at $z = -z_e$ or $z = -z_e + 3$ mm.

3 Small-domain LES/PDF simulations

The LES/PDF simulations are performed on the small cylindrical computational domain shown in Fig. 1(c). In this section a brief description of the computational methodology is presented followed by a discussion on the important simulation parameters for the three modes. Finally, the LES/PDF simulation results for the three modes are presented and discussed. For simplicity, henceforth, the LES/PDF simulations on the small domain are referred to as just the LES/PDF simulations.

3.1 Computational methodology

For the simulations involving the small cylindrical computational domain (see Fig. 1(c)), we employ the LES/PDF methodology through the coupled NGA/HPDF code [20–23]. The LES approach is used to treat the flow and turbulence [14, 15], while the PDF approach is used to treat the chemistry and the turbulence-chemistry interactions [16]. The finite-difference code (NGA [20]) is used to solve the LES equations in cylindrical coordinates and the PDF code (HPDF [21]) implementing a particle/mesh method is used to solve the PDF transport equations. The turbulent viscosity is obtained using the Lagrangian dynamic sub-grid scale model [24], and the dynamic model is applied on the mixture fraction (a conserved scalar) field to obtain the turbulent diffusivity. A random walk implementation for the molecular transport is employed along with the classical Interaction by Exchange with the Mean (IEM) mixing model [25]. All species diffusivities are taken to be equal to the thermal diffusivity under the unity Lewis number assumption. More details of the methodology and code implementation can be found in [14–16, 20–23].

For the reactive case considered (a non-premixed flame of the F/O mode), a 16-species Augmented Reduced Mechanism (ARM1) for methane oxidation [26] is used to represent the species and chemical reactions. For the I/B mode, the fluid is taken to be an inert ideal gas mixture.

3.2 Simulation parameters

Table 1 summarizes the important LES/PDF simulation parameters associated with the three modes of operation of the TCF burner. The bulk axial velocities for the two nozzles in the I/I mode are 6.58 m/s, while in the F/O mode they are at a higher value of 11.2 m/s. In the I/B mode, the inert stream has a bulk axial velocity of 11.2 m/s, whereas the hot product stream has a bulk axial velocity of 38.2 m/s. The higher value for the low-density product stream is set to shift the mean stagnation plane closer to the mid-plane between the two nozzles.

The bulk Reynolds number Re is defined as:

$$Re = \frac{U_{bulk} d_{jet}}{\nu_{N_2}}, \quad (10)$$

where U_{bulk} is the bulk axial velocity in the top nozzle and ν_{N_2} is the kinematic viscosity of N_2 at 294 K and 1 atm. The values of Re for the three modes are approximately 5500, 9400 and 9400, respectively.

Based on the bulk axial velocity U_{bulk} in the top jet, the bulk strain rate K_{bulk} is defined as:

$$K_{bulk} = \frac{2U_{bulk}}{d}. \quad (11)$$

The values of K_{bulk} for the three modes are approximately 1050, 1400 and 1200 1/s, respectively. In addition to U_{bulk} , the distance d between the two nozzles is also varied with values of 12.7, 16 and 19 mm for the three modes, respectively.

The turbulent Reynolds number Re_t is defined as:

$$Re_t = \frac{u'l'}{\nu_{N_2}}, \quad (12)$$

Table 1: Simulation parameters in the LES/PDF simulations of the three modes.

Parameter	Inert/Inert	Inert/Burnt	Fuel/Oxidant
Nozzle exit diameter (mm), d_{jet}	12.7	12.7	12.7
Distance between nozzles (mm), d	12.7	16	19
Computational domain: height, diameter (mm)	12.7, 60	16, 60	19, 60
Top stream	N_2	N_2	O_2
Bottom stream	N_2	Hot products	CH_4/N_2
Bulk axial velocity in the streams ^a (m/s), U_{bulk}	6.58	11.2; 38.2	11.2
Co-flow bulk velocity (m/s)	0.43	2.1	1.73
Bulk Reynolds number, Re	5500	9400	9400
Bulk strain rate (1/s), K_{bulk}	1050	1400	1200
Turbulent Reynolds number, Re_t	650	1050	750
Temperature of the streams ^a (K)	294	294; 1850	294
Grid size ($z \times r \times \theta$)	$96 \times 96 \times 32$	$96 \times 96 \times 32$	$144 \times 96 \times 32$
Total number of cells, particles	0.3M, 6M	0.3M, 6M	0.45M, 9M
Computational wall-clock time ($\mu s/cell/timestep$), (NGA%-HPDF%)	~ 16 (24%-76%)	~ 26 (30%-70%)	~ 20 (17%-83%)

^a The numerical values in each column are for the top and bottom streams, respectively. Single values are common for both the streams.

where u' and l' are the r.m.s. axial velocity and the longitudinal integral length scale, respectively. In the experiments, the turbulence intensity and the integral length scale are measured at a distance of 0.5 mm downstream of the top nozzle. The turbulent Reynolds number Re_t is varied by changing the position of the TGP inside the nozzle relative to the start of the nozzle contraction. It is observed in the experiments that the closer the TGP is to the contraction, the higher the intensity of turbulence at the nozzle exit. The values of Re_t for the three modes are approximately 650, 1050 and 750, respectively.

The grid sizes used in the LES/PDF simulations of the non-reactive cases (I/I and I/B modes) and the non-premixed case (F/O mode) are $96 \times 96 \times 32$ and $144 \times 96 \times 32$ in the axial, radial and azimuthal directions, respectively. This corresponds to a total number of grid cells of approximately 0.3M and 0.45M; and with 20 particles per cell, a total of approximately 6M and 9M particles are used in the HPDF code for the non-reactive and non-premixed cases, respectively. With the above grid sizes, the axial grid spacing Δ_z obtained in the simulations is approximately 0.13 mm. This value is lower than the grid resolution ($h = 0.5$ mm) used in the large-domain LES in Sec. 2.1. The simulations are run on NICS Kraken and Darter clusters using up to 64 cores. The particle code consumes at least $\sim 70\%$ of the total computational time; approximate wall-clock times (per computational cell, per time step) are shown in Table 1.

In order to reach a statistically-stationary state and to collect statistics, the LES/PDF simulations are advanced for a typical physical time of at least 0.05 s from initial conditions. This physical time corresponds to at least 25 flow-through times for all three modes, where one flow-through time is defined as the time taken for a fluid particle to travel the distance d between the two nozzles with the bulk velocity U_{bulk} . The average time step sizes used are 3×10^{-6} , 1×10^{-6} and 2×10^{-6} s for the I/I, I/B and F/O modes, respectively, which each give a value of under 0.4 for the Courant-Friedrichs-Lewy (CFL) number.

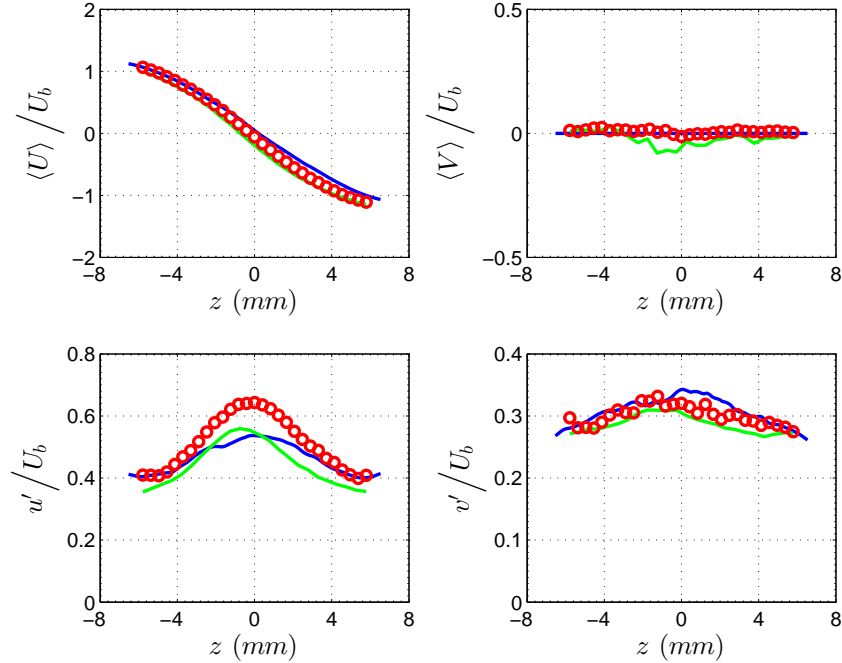


Fig. 4: The centerline profiles of the mean (top row) and r.m.s. (bottom row) axial and radial velocities for the I/I mode; blue line: small-domain LES/PDF simulation, green line: large-domain LES (Sec. 2.1), red symbols: experimental data [12]. The value of U_b is 6.58 m/s.

3.3 Results for the Inert/Inert (I/I) mode

Figure 4 compares the mean and r.m.s. axial and radial velocities on the burner centerline obtained from the LES/PDF simulations for the I/I mode with the results from the large-domain LES and the experimental data. Note that all the centerline plots are shown in such a way that the bottom nozzle stream is on the LHS and the top nozzle stream is on the RHS. The mean profiles are predicted very well by both the simulations. While the LES/PDF simulation predicts the stagnation plane to be at the mid-plane, the large-domain LES has the stagnation plane shifted slightly towards the left side. Both simulations under-predict the axial r.m.s. velocity at the stagnation plane by about 15%; however, there is a good match for the radial r.m.s. velocity. The maximum for the axial r.m.s. velocity is achieved at the mid-plane where as the r.m.s. of the radial velocity is fairly uniform along the centerline.

3.4 Results for the Inert/Burnt (I/B) mode

Figure 5 compares the centerline profiles of the mean and r.m.s. axial and radial velocity components obtained from the LES/PDF simulations for the I/B mode, for Case I (with no artificial turbulence imposed at $z = -z_e$), and Case II (with artificial turbulence at $z = -z_e$), with the experimental data. Note that the hot combustion product stream is on the LHS and the cold N_2 stream is on the RHS in the centerline plots.

There is no marked difference between the mean axial velocity profiles for the two cases and they match very well with the experimental data. The mean stagnation plane is at the mid-plane, as was intended by the suitable choice of the mean radial velocity profile at the bottom nozzle exit. The mean axial velocity on the hot combustion products stream side at

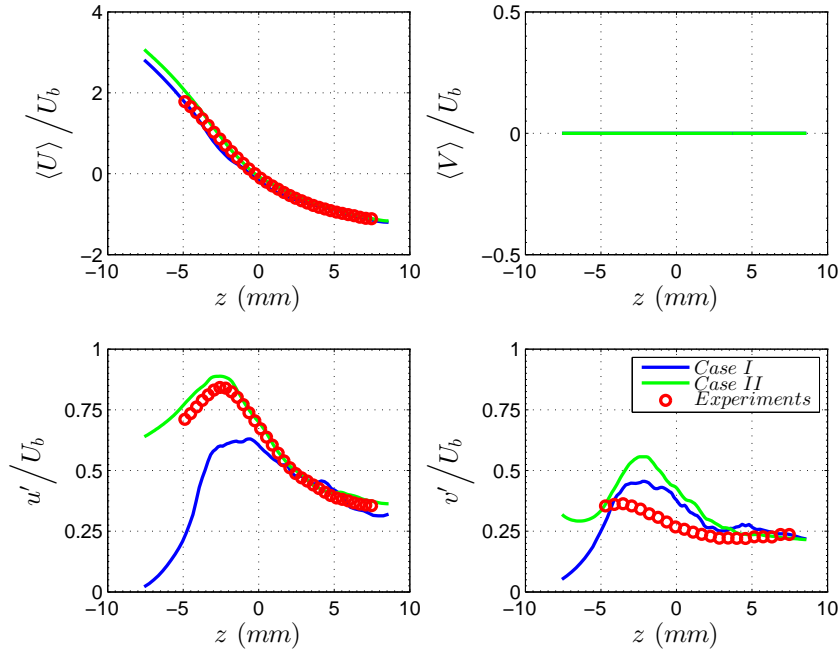


Fig. 5: The centerline profiles of the mean (top row) and r.m.s. (bottom row) axial and radial velocities for the I/B mode; blue line: LES/PDF simulations for Case I, green line: LES/PDF simulations for Case II, red symbols: experimental data [13]. Artificial turbulence is imposed at the bottom nozzle exit plane for Case II but not for Case I. The hot product stream is on the LHS and the inert N_2 stream is on the RHS. The value of U_b is 11.2 m/s.

$z = -5$ mm (i.e., $z = -z_e + 3$ mm) in Fig. 5 reaches twice the value of that on the inert N_2 stream side (i.e., $z = z_e$).

The key difference between the two cases can be seen in the prediction of the r.m.s. axial velocity. In Case I, this quantity is considerably under-predicted at the mid-plane (by about 25%) and, as prescribed, drops to zero at the bottom nozzle exit plane. On the other hand, Case II better predicts the r.m.s. axial velocity at the mid-plane due to the prescribed non-zero value of this quantity at the bottom nozzle exit plane. It should be noted that both cases over-predict the r.m.s. radial velocity, especially near the mid-plane (by about 30% for Case I and 60% for Case II). The maxima of r.m.s. axial and radial velocity components are reached on the hot product stream side, both in the simulations and experiments.

It is also important to consider the radial profiles of the mean and r.m.s. axial and radial velocities at a distance of 3 mm above the bottom nozzle exit plane (i.e., $z = -z_e + 3$ mm) to differentiate between the two cases. Figure 6 shows these profiles for the two cases and their comparison to the experimental data. As is evident from this figure, there is a small difference in the radial profiles of the mean quantities, but as expected, we see major differences in the prediction of the r.m.s. quantities for the two cases. In general, Case II performs better than Case I as the predicted profiles for the r.m.s. quantities are closer to the experimental data. The experimental data at $z = -z_e + 3$ mm are key in determining the velocity inflow boundary conditions at the bottom nozzle exit plane (i.e., $z = -z_e$), which highlights the importance of the availability of experimental data close to the nozzle exits for a better prediction of the TCF flow and flame using the velocity inflow methodology described in this paper.

Finally, we compare instantaneous contour plots of the axial velocity from the two cases on a plane cutting the solution domain through the center. Case I is shown in Fig. 7(a) and Case II is shown in Fig. 7(b). A clear understanding of the flow development in the two cases can be visualized through these contour plots. To reiterate, artificial turbulence is imposed

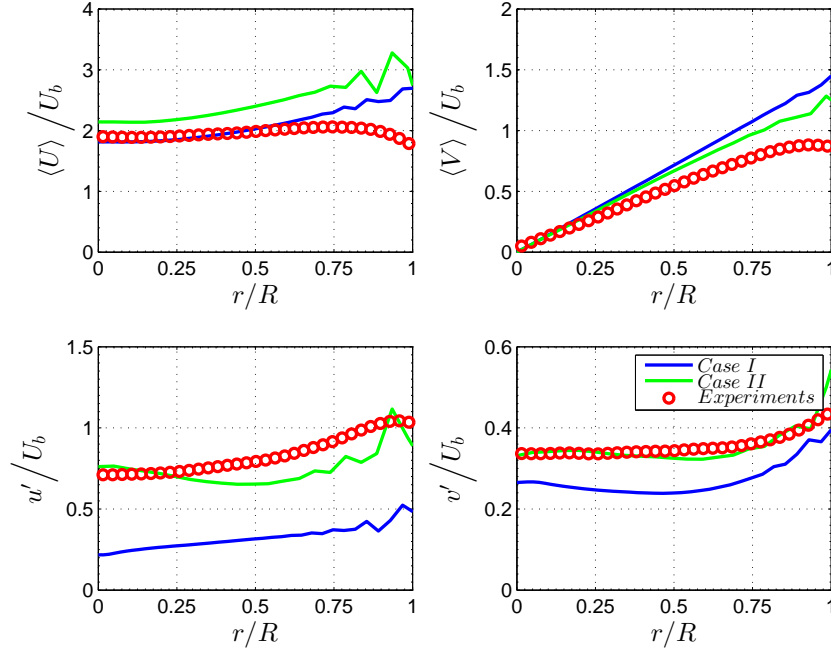


Fig. 6: The radial profiles of the mean (top row) and r.m.s. (bottom row) axial and radial velocities for the I/B mode at a distance of 3 mm above the bottom nozzle exit plane (i.e., $z = -z_e + 3$ mm); blue line: LES/PDF simulations for Case I, green line: LES/PDF simulations for Case II, red symbols: experimental data [13]. Artificial turbulence is imposed at the bottom nozzle exit plane for Case II but not for Case I. The hot product stream is on the LHS and the inert N_2 stream is on the RHS. The value of U_b is 11.2 m/s.

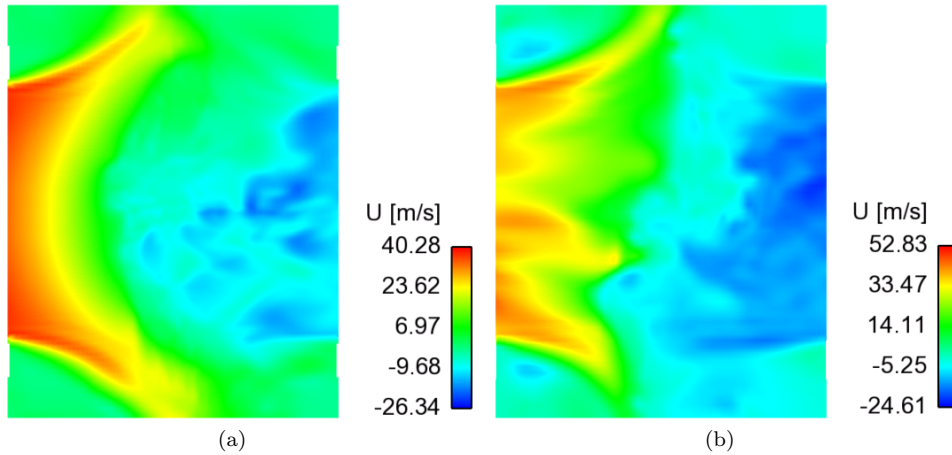


Fig. 7: Instantaneous contour plots of the axial velocity on a plane intersecting the solution domain through the center for (a) Case I with no artificial turbulence at the bottom nozzle exit plane and (b) Case II with artificial turbulence at the bottom nozzle exit plane. The hot product stream is on the LHS and the inert N_2 stream is on the RHS.

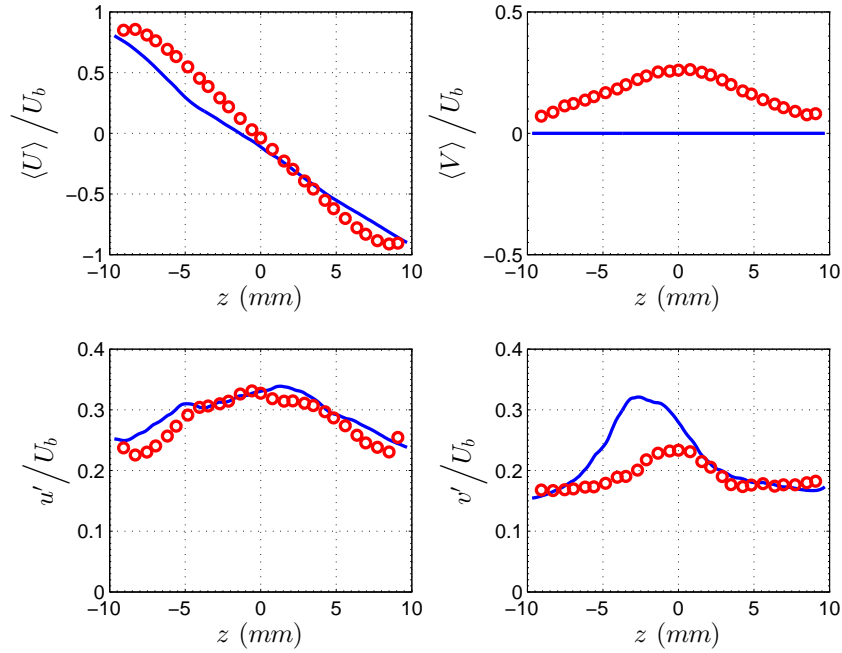


Fig. 8: The centerline profiles of the mean (top row) and r.m.s. (bottom row) axial and radial velocities for the F/O mode; blue line: LES/PDF simulation, red symbols: experimental data [12]. The fuel stream CH_4/N_2 is on the LHS and the oxidant stream O_2 is on the RHS. The value of U_b is 11.2 m/s.

(refer to Sec. 2.5) at the bottom nozzle exit plane in Case II, whereas the N_2 stream (RHS) is turbulent in nature in both the cases. This difference in the nature of the velocity field at the bottom nozzle exit plane has a profound effect on the flow field development between the two nozzles.

3.5 Results for the Fuel/Oxidant (F/O) mode

Figure 8 shows the same velocity statistics on the centerline between the two nozzle exits for the non-premixed reactive case. The fuel stream is on the LHS and the oxidant stream is on the RHS. We infer that the prediction of the mean axial velocity is satisfactory. Symmetry is expected for the mean radial velocity and the LES/PDF simulations predict it to be zero on the centerline, but some asymmetry is observed in the experimental data.

The axial r.m.s. velocity is well-predicted along the centerline with the maximum occurring near the mid-plane. However, the radial r.m.s. velocity has a predicted maximum towards the fuel side in the simulations and is over-predicted by about 35%. This is comparable to the fuel-side shift and over-estimation of peak radial r.m.s. velocity in the large-domain LES results presented in [12].

Additionally, we look at the radial profiles of the mean and r.m.s. of the two velocity components from the LES/PDF simulations at 0.5 mm downstream of the nozzle exit planes (i.e., $z = \mp z_e \pm 0.5$ mm) to gauge the performance of the inflow boundary conditions method. Figure 9(a) shows the profiles at $z = -z_e + 0.5$ mm (fuel stream side) and Fig. 9(b) shows the profiles at $z = z_e - 0.5$ mm (oxidant stream side). It can be inferred that the inflow method is able to specify the velocity time series data at the exit planes accurately so that the radial profiles extracted from the LES/PDF simulations agree well with the experimental data at 0.5 mm downstream of the nozzle exits.

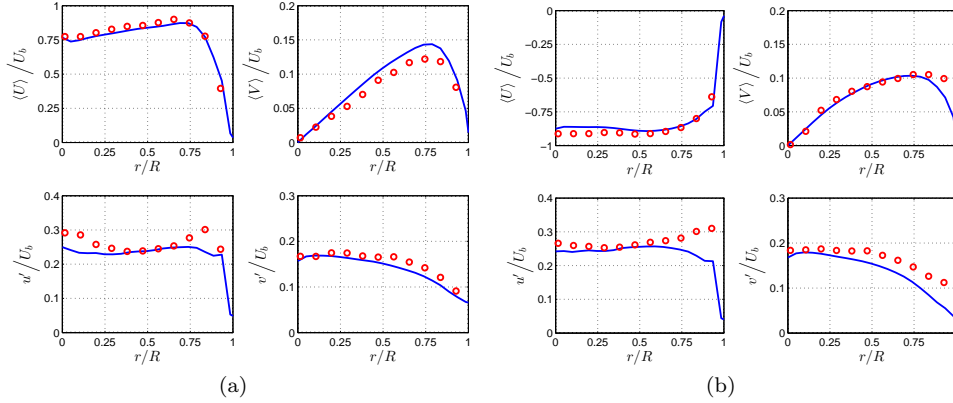


Fig. 9: The radial profiles of the mean (top row) and r.m.s. (bottom row) axial and radial velocities at a distance of 0.5 mm downstream of (a) the fuel stream nozzle exit plane (i.e., $z = -z_e + 0.5$ mm) and (b) the oxidant stream nozzle exit plane (i.e., $z = z_e - 0.5$ mm) for the F/O mode; blue line: LES/PDF simulation, red symbols: experimental data [12]. The value of U_b is 11.2 m/s.

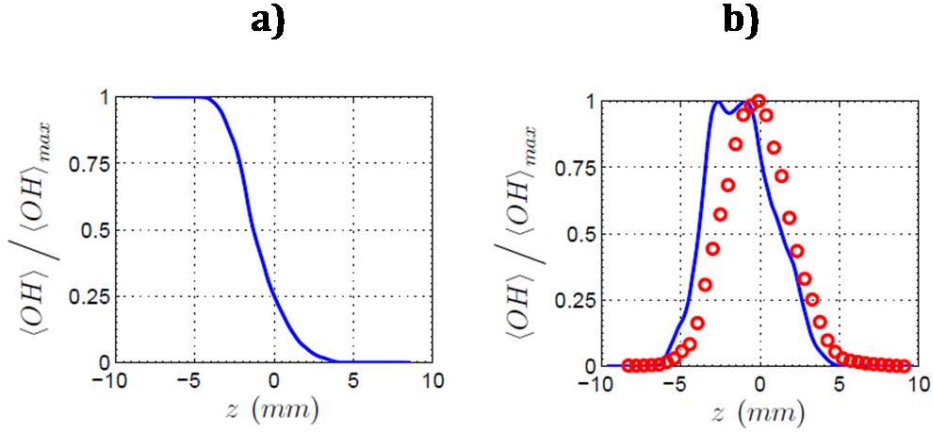


Fig. 10: The centerline profiles of the normalized mean OH species mass fraction for (a) the I/B mode, Case II and (b) the F/O mode; blue line: LES/PDF simulation, red symbols: experimental data [12]. For the I/B mode, the hot product stream is on the LHS and the inert N_2 stream is on the RHS. For the F/O mode, the fuel stream is on the LHS and the oxidant stream is on the RHS.

Finally we look at the normalized mean OH species mass fraction on the centerline for the I/B and F/O modes. Since Case II generally provides a better match with velocity statistics from experiments, the mean profile from Case II only is considered and shown in Fig. 10(a). Due to the lack of experimental data for the temperature and many of the species mass fractions, we are only able to compare the normalized mean OH mass fraction profile on the centerline for the F/O mode as shown in Fig. 10(b). The comparison is good, although the non-premixed flame predicted by the LES/PDF simulation is slightly towards the fuel nozzle stream side. As is evident from Fig. 10, the mean OH profiles are very different for the two modes. In the I/B mode, the peak in the profile occurs at the LHS (hot product stream

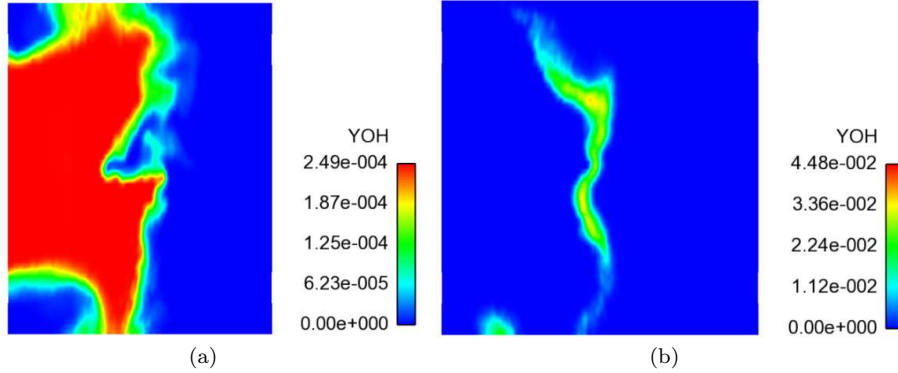


Fig. 11: Instantaneous contour plots of the OH species mass fraction on a plane intersecting the solution domain through the center for (a) the I/B mode, Case II and (b) the F/O mode. For the I/B mode, the hot product stream is on the LHS and the inert N_2 stream is on the RHS. For the F/O mode, the fuel stream is on the LHS and the oxidant stream is on the RHS.

nozzle exit) and goes to 0 at the RHS (N_2 stream nozzle exit), whereas for the F/O mode, the peak occurs between the two nozzles due to the formation of the non-premixed flame that is established near the mid-plane.

This observation is also made clear by the instantaneous contour plots of OH species mass fraction, shown in Figs. 11(a) and 11(b) for the I/B and F/O modes, on a plane intersecting the solution domain through the center. The peak values of OH species are very different in the two modes. In the I/B mode, peak OH is determined by the equilibrium composition of the product stream at $T_b = 1850$ K; in the F/O mode, it is determined by the combustion processes leading to the formation of the non-premixed flame.

4 Conclusions

The following conclusions can be drawn from the results presented in this work:

- Broadly, two types of solution domain can be employed in computational studies of the turbulent counterflow configuration: (i) a large domain that includes the entire region between the two TGPs within the nozzles and (ii) a small cylindrical domain that excludes the regions downstream of the TGPs and only includes the region between the two nozzle exit planes.
- The large-domain high-fidelity LES allows for the prediction of development of the non-trivial, high-intensity turbulent velocity field downstream of the TGP but is computationally quite expensive.
- The LES/PDF simulations on the small cylindrical domain are simpler in terms of the simulated geometry and less expensive. However, the inflow boundary conditions for the velocity field need to be known *a priori*.
- A new inflow boundary condition method is developed to specify the time series of the turbulent velocity fields at the nozzle exit planes for small-domain simulations.
- The three key ingredients of the inflow methodology are: (i) a single large-domain LES to record the time series of the velocity fields on the nozzle exit planes, (ii) experimental data at (or close to) the nozzle exit planes, and (iii) a transformation procedure that is applied on the recorded time series data so as to match the mean and r.m.s. of the velocity components and the longitudinal integral length scale on the centerline at the nozzle exit

plane, and hence the turbulent Reynolds number Re_t , in the simulations to that of the experiments.

- The inflow method is assessed by implementing it in the LES/PDF simulations of three different modes of operation of the TCF burner.
- The method is found to be successful in predicting the first and second moments of the axial and radial velocities on the centerline connecting the two jets for all the modes.
- Finally, it is proposed that this simple yet robust inflow methodology can be efficiently used in LES/PDF simulations to conduct a parametric study on the premixed mode of the TCF configuration, which is experimentally studied in [13].

Acknowledgements We are grateful to Dr. B. Coriton for providing the experimental data for all the modes described in this work. We also gratefully acknowledge the California Institute of Technology, the University of Colorado at Boulder and Stanford University for licensing the NGA code used in this work.

The authors thank the University of Tennessee and Oak Ridge National Laboratory Joint Institute for Computational Sciences and Cornell University Center for Advanced Computing for providing the computational resources required to perform this work.

Funding

This work is supported by the U.S. Department of Energy, Office of Science, Office of Basic Energy Sciences under award number DE-FG02-90 ER14128. This work used the Extreme Science and Engineering Discovery Environment (XSEDE), which is supported by National Science Foundation grant number ACI-1053575.

References

1. L. W. Kostiuk, K. N. C. Bray, and T. C. Chew. Premixed turbulent combustion in counterflowing streams. *Combust. Sci. and Tech.*, 64:233–241, 1989.
2. E. Mastorakos, A. M. K. P. Taylor, and J. H. Whitelaw. Extinction and temperature characteristics of turbulent counterflow diffusion flames with partial premixing. *Combust. Flame*, 91:40–54, 1992.
3. L. W. Kostiuk, K. N. C. Bray, and R. K. Cheng. Experimental study of premixed turbulent combustion in opposed streams. Part II—reacting flow field and extinction. *Combust. Flame*, 92:396–409, 1993.
4. D. Geyer, A. Kempf, A. Dreizler, and J. Janicka. Turbulent opposed-jet flames: A critical benchmark experiment for combustion LES. *Combust. Flame*, 143:524–548, 2005.
5. G. Coppola, B. Coriton, and A. Gomez. Highly turbulent counterflow flames: A laboratory scale benchmark for practical systems. *Combust. Flame*, 156:1834–1843, 2009.
6. A. Gomez. Highly turbulent counterflow flames: A laboratory-scale benchmark for turbulent combustion studies. Technical report, Fall Technical Meeting of the Eastern States Section of the Combustion Institute, 2011.
7. P. Geipel, K. H. H. Goh, and R. P. Lindstedt. Fractal-generated turbulence in opposed jet flows. *Flow Turbul. Combust.*, 85:397–419, 2010.
8. K. H. H. Goh, P. Geipel, and R. P. Lindstedt. Lean premixed opposed jet flames in fractal grid generated multiscale turbulence. *Combust. Flame*, 161:2419–2434, 2014.
9. J. Eckstein, J. Y. Chen, C. P. Chou, and J. Janicka. Modeling of turbulent mixing in opposed jet configuration: one-dimensional Monte Carlo probability density function simulation. *Proc. Combust. Inst.*, 28:141–148, 2000.
10. I. S. Kim and E. Mastorakos. Simulations of turbulent non-premixed counterflow flames with first-order conditional moment closure. *Flow Turbul. Combust.*, 76:133–162, 2006.
11. R. P. Lindstedt, D. S. Luff, and J. H. Whitelaw. Velocity fields of fuel lean premixed turbulent opposed jet flames. *Proc. Combust. Inst.*, 31:1459–1466, 2007.
12. M. W. A. Pettit, B. Coriton, A. Gomez, and A. M. Kempf. Large-eddy simulation and experiments on non-premixed highly turbulent opposed jet flows. *Proc. Combust. Inst.*, 33:1391–1399, 2011.

13. B. Coriton, J. H. Frank, and A. Gomez. Effects of strain rate, turbulence, reactant stoichiometry and heat losses on the interaction of turbulent premixed flames with stoichiometric counterflowing combustion products. *Combust. Flame*, 160:2442–2456, 2013.
14. S. B. Pope. *Turbulent Flows*. Cambridge University Press, Cambridge, 2000.
15. H. Pitsch. Large-eddy simulation of turbulent combustion. *Annu. Rev. Fluid. Mech.*, 38:453–482, 2006.
16. S. B. Pope. PDF methods for turbulent reactive flows. *Prog. Energy Combust. Sci.*, 11:119–192, 1985.
17. G. Coppola and A. Gomez. Experimental investigation on a turbulence generation system with high-blockage plates. *Exp. Therm. Fluid Sci.*, 33:1037–1048, 2009.
18. D. Geyer, A. Dreizler, J. Janicka, A. D. Permana, and J. Y. Chen. Finite-rate chemistry effects in turbulent opposed flows: comparison of Raman/Rayleigh measurements and Monte Carlo PDF simulations. *Proc. Combust. Inst.*, 30:711–718, 2005.
19. A. Kempf, H. Forkel, J. Y. Chen, A. Sadiki, and J. Janicka. Large-eddy simulation of a counterflow configuration with and without combustion. *Proc. Combust. Inst.*, 28:35–40, 2000.
20. O. Desjardins, G. Blanquart, G. Balarac, and H. Pitsch. High order conservative finite difference scheme for variable density low mach number turbulent flows. *J. Comput. Phys.*, 227:7125–7159, 2008.
21. H. Wang and S. B. Pope. Large-eddy simulation/probability density function modeling of a turbulent CH₄/H₂/N₂ jet flame. *Proc. Combust. Inst.*, 33:1319–1330, 2011.
22. Y. Yang, H. Wang, S. B. Pope, and J. H. Chen. Large-eddy simulation/probability density function modeling of a non-premixed CO/H₂ temporally evolving jet flame. *Proc. Combust. Inst.*, 34:1241–1249, 2013.
23. S. B. Pope. Computationally efficient implementation of combustion chemistry using in situ adaptive tabulation. *Combust. Theor. Model.*, 1:41–63, 1997.
24. C. Meneveau, T. S. Lund, and W. H. Cabot. A lagrangian dynamic subgrid-scale model of turbulence. *J. Fluid Mech.*, 319:353–385, 1996.
25. J. Villiermaux and J. C. Devillon. Représentation de la coalescence et de la redispersion des domaines de ségrégation dans un fluide par un modèle d’interaction phénoménologique. In *Proc. 2nd Int. Symp. Chem. React. Eng.*, pages 1–13, New York, 1972. Elsevier.
26. C. J. Sung, C. K. Law, and J. Y. Chen. An augmented reduced mechanism for methane oxidation with comprehensive global parametric validation. *Proc. Combust. Inst.*, 27:295–304, 1998.